

See discussions, stats, and author profiles for this publication at: <https://www.researchgate.net/publication/244461684>

Structural Features of SnO₂ Nanowires and Raman Spectroscopy Analysis

ARTICLE *in* CRYSTAL GROWTH & DESIGN · SEPTEMBER 2009

Impact Factor: 4.89 · DOI: 10.1021/cg9000957

CITATIONS

30

READS

103

5 AUTHORS, INCLUDING:



Dah-Shyang Tsai

National Taiwan University of Science and T...

144 PUBLICATIONS 1,791 CITATIONS

SEE PROFILE



Chen-Chia Chou

National Taiwan University of Science and T...

157 PUBLICATIONS 825 CITATIONS

SEE PROFILE



ying-sheng Huang

National Taiwan University of Science and T...

1,053 PUBLICATIONS 18,735 CITATIONS

SEE PROFILE

Structural Features of SnO₂ Nanowires and Raman Spectroscopy Analysis

Adrianus Leonardy,[†] Wen-Zhong Hung,[†] Dah-Shyang Tsai,^{*,†} Chen-Chia Chou,[‡] and Ying-Sheng Huang[§]

[†]Department of Chemical Engineering and [‡]Department of Mechanical Engineering and [§]Department of Electronic Engineering, National Taiwan University of Science and Technology, Taipei 10607 Taiwan

Received January 25, 2009; Revised Manuscript Received June 10, 2009

ABSTRACT: Tilted SnO₂ nanowires (SnO₂NW) have been grown and aligned on the sapphire (SA) substrate of orientation (100) or (110). Their structural and spectroscopic features are studied using scanning electron microscopy, transmission electron microscopy, X-ray diffraction, and Raman spectroscopy, with the emphasis on the wire roots. On the SA(100) substrate, the (001) facet of SnO₂ preferentially matches the SA(100) plane. The longitudinal SnO₂ crystal grows in the [101] direction with the enclosing facets of {010} and {10 $\bar{1}$ }, which are perpendicular to form its rectangular cross-section. On the SA(110) substrate, the (101) facet of SnO₂ matches the SA(110) plane, and the wire crystal elongates in the [100] direction with the enclosing orthogonal facets of {010} and {001}. Because the angle between two SnO₂ facets (101) and (001) is 34°, the SnO₂NWs on SA(100) and (110) are tilted with an angle of ~56° from the substrate normal to the growth direction. The main difference between two SnO₂NWs is the planar alignment, which creates a rectangular grid pattern on SA(100) and a herringbone pattern on SA(110). We further demonstrate that the wire size, evaluated via fitting the line profile of Raman A_{1g} mode, can be controlled in the range of 30–80 nm through manipulating the sputtered thickness of gold layer on both substrates.

1. Introduction

The intriguing properties of SnO₂ nanowires (SnO₂NW) promise extensive applications in gas sensing, electronics, and photonics. Their physical and chemical characteristics are intimately associated with the nanometer size, geometric shape, and enclosing crystallographic facets, which are major structural variants in regulating the properties. SnO₂ is a wide bandgap (3.6 eV) semiconductor that crystallizes in the tetragonal rutile structure ($a = 4.737 \text{ \AA}$, $c = 3.186 \text{ \AA}$) with space group $P4_2/mnm$.¹ SnO₂ is generally regarded as the material for gas sensing, because of its high reversibility and sensitivity in adsorbing the reducing and oxidizing gases. The potential applications of SnO₂NW involve chemical sensors,^{2–9} transistors,¹⁰ and field emitters.^{11,12} The nanowires have mostly been grown using the gas-phase techniques, such as thermal evaporation of SnO, Sn metal, mixtures of SnO₂ and carbon,^{10,13–16} chemical vapor deposition with the tin butoxide precursor,¹⁷ and laser ablation.¹⁸ Other forms of SnO₂ nanocrystals are also grown using wet chemistry techniques, such as hydrothermal techniques^{5,19,20} and electrochemical deposition, followed by oxidation in anodic alumina membrane²¹ and solution-phase synthesis.^{22,23}

A prevalent method in preparing the SnO₂ nanowires is to grow these one-dimensional crystals via the vapor–liquid–solid (VLS) mechanism, assisted by the gold catalysts. The method produces thin nanobelts or nanowires of tiny dimensions and clearly defined geometry, suggesting the capability of VLS mechanism in controlling the crystal dimensions. Despite its widespread popularity, only a few reports in the literature discussed how to manipulate the structural features

of SnO₂ nanowires, especially when they were grown on the single-crystalline substrate.^{17,24} In this work, we grow SnO₂NWs on two sapphire substrates, using the dewetted gold particles as the nucleation agent. The average wire size is controlled by regulating the thickness of gold layer, and analyzed with the Raman spectroscopy. The epitaxial relation, enclosed crystallographic facets, and growth direction are analyzed and discussed, using X-ray diffraction (XRD), scanning electron microscopy (SEM), and transmission electron microscopy (TEM).

2. Experimental Details

The growth of SnO₂NW was carried out in a horizontal alumina tube of three inches in diameter, heated by a Lindberg furnace. The alumina tube was vacuum sealed by two water-cooled end pieces of stainless steel, tightly lock-press fit against the Viton O-rings. For the wire growth, high purity argon gas (99.999% purity, 10 sccm) entered through the upstream end piece and flowed over an alumina crucible containing the tin source of high-purity SnO powder (>99.9%, Acros). The evaporation temperature of SnO was kept at $700 \pm 2 \text{ }^\circ\text{C}$. The sapphire (SA) substrate of (100) or (110) orientation was placed on an alumina plate heated at $645 \pm 2 \text{ }^\circ\text{C}$, downstream of the tin source. The total pressure was controlled at 10 Torr by a mechanical pump that was connected to the downstream end piece. The SA substrates were cut in $\sim 10 \times 10 \text{ mm}^2$ pieces, cleansed with acetone and methanol consecutively in an ultrasonic bath for 10 min, and dried in a laminar-flow cabinet. Prior to the growth, the clean substrate of SA(100) or SA(110) was sputtered with a gold layer of known thickness through controlling the sputtering time, using an Emitech-K550 sputter coater. The substrate was then placed in the furnace, and the gold thin film dewetted at $400 \pm 2 \text{ }^\circ\text{C}$ (5 min) and formed a surface with the densely populated gold droplets for wire growth. The dewetting mechanism of Au had been studied on the silicon wafers.^{25,26}

The morphology of nanowires was examined using a field-emission scanning electron microscope (FESEM JSM6500F, JEOL). The crystalline phase and the preferred orientation of short wires were analyzed using an X-ray diffractometer (D/Max-RC, Rigaku), which

*Corresponding author. Address: Department of Chemical Engineering, National Taiwan University of Science and Technology, 43 Keelung Road, Section 4, Taipei 10607, Taiwan. E-mail: dstsai@mail.ntust.edu.tw. Phone: 886-2-27376618. FAX: 886-2-27376644.

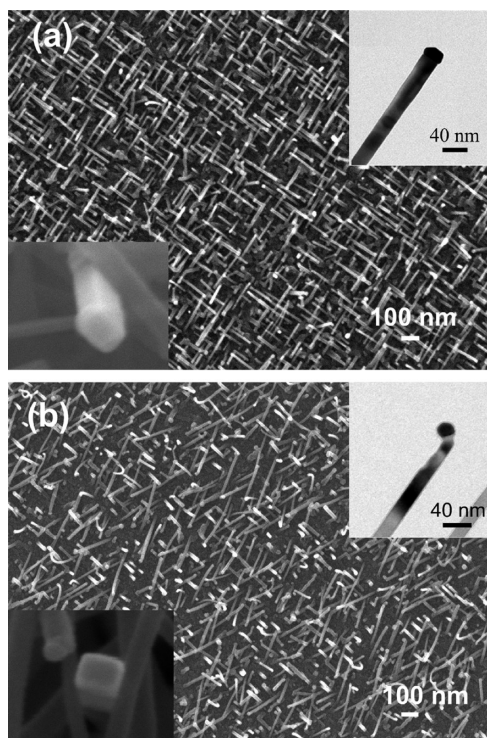


Figure 1. Top views of SnO_2NW grown on (a) SA(100) and (b) SA(110) substrates. Growth of nanowires was conducted at 645°C for 40 min on the substrates being sputtered Au for 20 s. Two SEM insets show that the rectangular cross-sections of wire are slightly different on the two substrates. Two TEM insets show that the wire size is nearly the same with its gold droplet on top.

was equipped with a Cu $K\alpha$ radiation source and a nickel filter. More structural details were revealed using a high-resolution transmission electron microscope HRTEM (Tecnai F20 G2, Philips-FEI) operated at 200 kV, equipped with a field emission gun and a double-tilt holder. Raman spectra were recorded in the backscattering mode at room temperature, using a Renishaw inVia micro-Raman system equipped with an 1800 grooves/mm grating and an optical microscope comprising a $50\times$ objective lens. The radiation source was an Ar^+ laser beam of wavelength 514.5 nm, which was focused on a spot of $5\ \mu\text{m}$ in size at 2.0 mW. Before measurement, the micro-Raman system was calibrated using the $520\ \text{cm}^{-1}$ peak of polycrystalline Si. Several samples of SnO_2 powder ($>99.9\%$, Aldrich) of rutile structure were thermally annealed at 1000°C for 8 h to grow their crystallite sizes. The Raman spectrum of the annealed SnO_2 powder was used as the reference in analyzing the size effect in Raman scattering, because the spectra of annealed samples longer than 8 h were virtually the same.

3. Results and Discussion

3.1. SEM and XRD Analysis. When the heteroepitaxial growth conditions are met and the wire length is restricted such that the wire is not too long to bend down or entangle itself with other wires, the organized pattern of SnO_2 nanowires will be visible. Figure 1 presents two distinct cross-hatching patterns formed by SnO_2NWs , which were grown on SA(100) and SA(110) at 645°C for 40 min. The orderly patterns from a bird's-eye view suggest the SnO_2 thin crystal tilts toward a few specific directions to match the surface symmetry of substrate. Two insets of secondary electron image show that these SnO_2 wires are rectangular and enclosed by well-defined facets. But the length-to-width ratio of cross-section appears to be different for the wires on SA(100) and SA(110). For most wires, a gold alloyed droplet

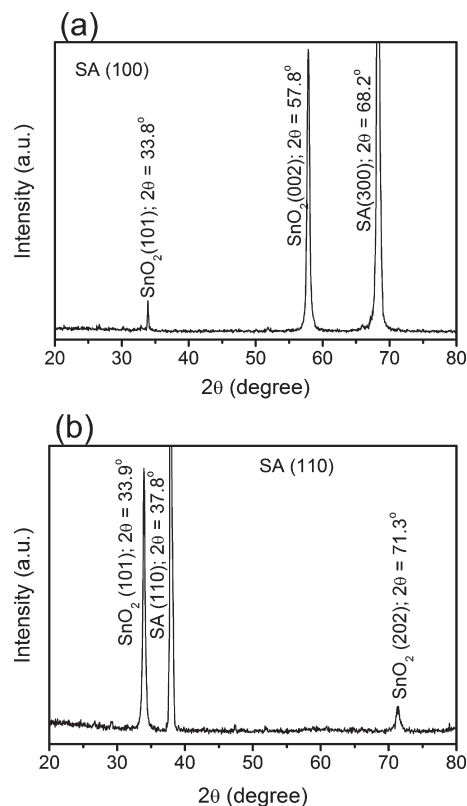


Figure 2. XRD patterns of SnO_2NW grown on (a) SA(100) and (b) SA(110) at 645°C for 20 min. The Au sputtering time was 20 s.

can usually be found at the head of growth front. In images a and b in Figure 1, two bright-field TEM insets show the typical gold droplets and the ensuing straight nanowires. The gold alloy seed may not be spherical in shape or right on top of the wire, but nearly the same size with the SnO_2 wire. The above observations indicate that the growth of SnO_2NW was mediated by the gold alloy droplet; meanwhile, the nanowires were aligned because of the epitaxy.

X-ray diffraction patterns of SnO_2NW reveal more structural details on the interfacing facets between the rutile and sapphire crystals. Figure 2a presents a clean XRD pattern of SnO_2NW on SA(100), comprising three peaks in the 2θ range of $20\text{--}80^\circ$. The most intense peak at 68.2° belongs to $\alpha\text{-Al}_2\text{O}_3$ (300) because of the sapphire substrate. The second most intense peak at 57.8° and a much weaker peak at 33.8° are the diffraction lines of SnO_2 (002) and (101) planes, respectively. The high intensity of the 57.8° line suggests the longitudinal crystal is constructed by stacking numerous SnO_2 (001) crystal planes upward. As for the minor SnO_2 -(101) line at 33.8° , the diffraction peak is considered to arise from the SnO_2 deposits on the sapphire surface, which failed to develop into nanowires. The diffraction pattern of SnO_2NW on SA(110) is plotted in Figure 2b, displaying a pair of diffraction peaks at 33.9 and 71.3° which are indexed as the (101) and (202) planes. The other strong diffraction line at 37.8° originates from the $\alpha\text{-Al}_2\text{O}_3$ (110) plane of the substrate. Thus we deduce the epitaxial relations for the two SnO_2NWs as follows; the crystal plane of SnO_2 (001) matches that of SA(100), whereas the plane of SnO_2 (101) matches that of SA(110).

3.2. TEM Analysis for Growth Direction and Enclosing Facets. The growth direction and the enclosing facets are investigated by tilting a rectangular wire in the TEM analy-

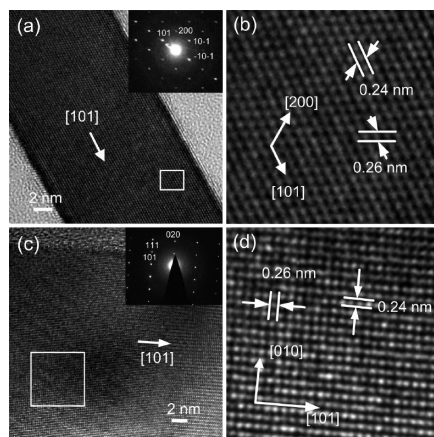


Figure 3. TEM images of two facets enclosing a SnO_2 nanowire grown on SA(100). For one facet of the nanowire, (a) the HRTEM image and its SAD pattern when viewing along the zone axis $[0\bar{1}0]$, and (b) an enlarged lattice image marked in (a). For the other facet of the nanowire, (c) the HRTEM image and its SAD pattern when viewing along the zone axis $[10\bar{1}]$, and (d) an enlarged lattice image selected in (c).

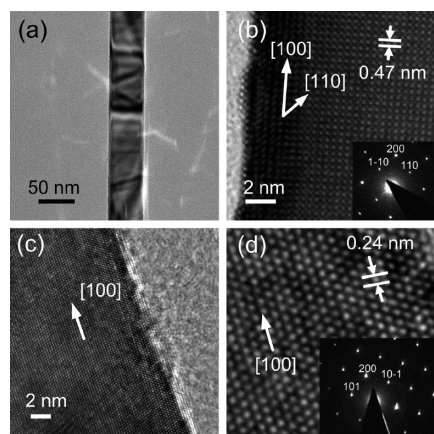


Figure 4. TEM images of two facets enclosing a SnO_2 nanowire grown on SA(110). For one side of the nanowire, (a) a bright-field image of the nanowire, (b) the lattice image of the wire and the SAD pattern when viewing along the zone axis $[001]$. For the other side of the nanowire, (c) the HRTEM image of zone axis $[010]$, and (d) an enlarged lattice image marked in (c) along with the SAD pattern.

sis. Figure 3a presents the HRTEM image of a SnO_2 wire grown on SA(100). The inset shows the selected area diffraction (SAD) pattern of the image, indicating the zone axis is $[0\bar{1}0]$. The HRTEM image of Figure 3b, taken from the marked region of Figure 3a, illustrates the clear lattice spacings between the adjacent planes of (101) and (200) . Hence this wire plane belongs to the $\{010\}$ facets. Images c and d in Figure 3 show a pair of HRTEM images for the other wire plane. The SAD pattern in Figure 3c indicates the image is taken when viewing along the zone axis of $[10\bar{1}]$. With the clear lattice spacings of (101) and (020) , we identify this wire plane as belonging to the $\{\bar{1}01\}$ facets. Because the $\{\bar{1}01\}$ facets of rutile crystal are perpendicular to the $\{010\}$ facets, the two identified facets do form a rectangular enclosure for the wire. To find the wire direction, we apply the technique of trace analysis and conclude the growth direction of nanowires on SA(100) is $[101]$. This growth direction of SnO_2 NW appears to be quite common, it has been reported in the literature of SnO_2 nanowires.^{13–15}

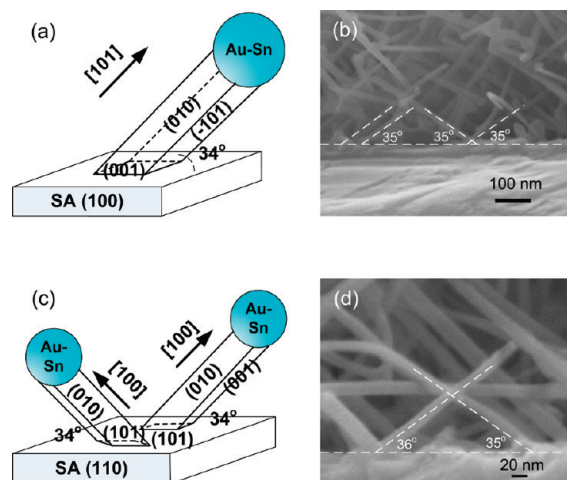


Figure 5. Two schematic diagrams for enclosing facets of the SnO_2 nanowire grown on (a) SA(100) and (c) SA(110). A cross-sectional view of tilted nanowires, which were grown on (b) SA(100) and (d) SA(110), with their tilt angles marked. The Au sputtering time was 20 s.

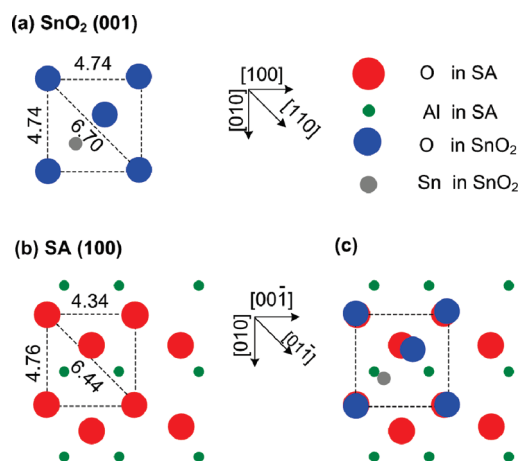


Figure 6. Schematic diagram of the lattice relation between SnO_2 -(001) and SA(100). The surface lattice is drawn for (a) SnO_2 -(001), (b) SA(100), (c) SnO_2 -(001) on top of SA(100).

Figure 4a presents the bright-field image of a wire chosen from the SnO_2 NW on SA(110). Figure 4b depicts the HRTEM image of one facet of the wire, along with its SAD pattern corresponding to the zone axis of $[001]$. Judging from the SAD pattern and the lattice spacings, we deduce the facet of the wire belongs to $\{001\}$. The HRTEM images of the other facet of the wire are illustrated in images c and d in Figure 4. The SAD pattern indicates that the zone axis is $[010]$ and the facet belongs to $\{010\}$. Similarly, we infer the growth direction of nanowires on SA(110) to be $[100]$, and the wire is enclosed by $(0\bar{1}0)$, (010) , (001) , and $(00\bar{1})$ perpendicular facets.

A schematic diagram, as shown in Figure 5a, summarizes the discussion on the crystallographic facets of SnO_2 NW on SA(100). The wire of SnO_2 NW on SA(100) grows in the $[101]$ direction and is enclosed by the $(0\bar{1}0)$, (010) , $(10\bar{1})$, and $(\bar{1}01)$ facets. The nanowire is expected to tilt with respect to the substrate at an angle of 34° , because the angle between the growth direction $[101]$ and the normal of SnO_2 (001) is 56° . The tilt angle is confirmed in Figure 5b, showing an angle of $\sim 35^\circ$ near the wire roots. The wires could tilt to the right or

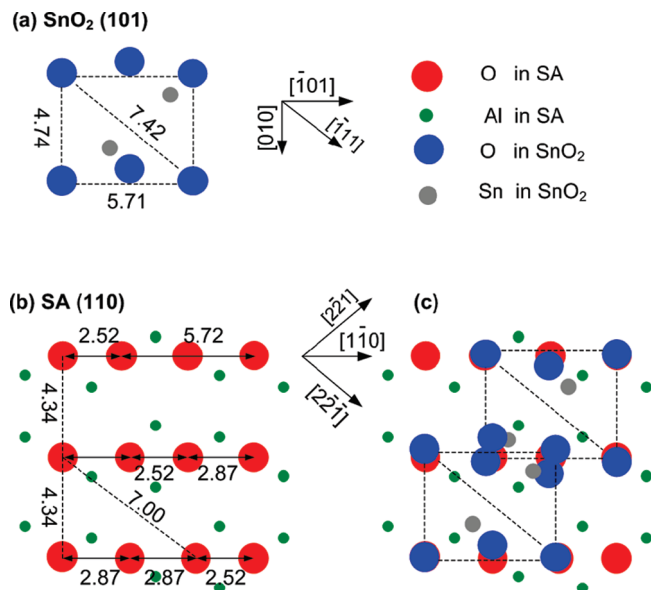


Figure 7. Schematic diagram of the lattice relation between SnO₂-(101) and SA (110). The surface lattice is drawn for (a) SnO₂(101), (b) SA(110), and (c) SnO₂(101) on top of SA(110).

the left with analogous opportunity. Likewise, Figure 5c summarizes the enclosing facets for the nanowires on SA(110). The tilt angle should be 34°, which is the angle between two SnO₂ facets of (001) and (101). The SEM image of Figure 5d verifies the tilt angle with an isosceles triangle formed by two tilted wires of inclination angle 35 and 36°. For the two SnO₂NWs on SA(100) and (110), they are both enclosed by {010}, but differ in {101} and {001} facets.

The planar alignment of SnO₂ wires on the sapphire substrate is further analyzed, assuming the SA surface is terminated by the oxygen atoms and the surface lattice offers a template for the crystal growth. The atomic template of SA(100) is illustrated in Figure 6b, which shows the periodicity of every oxygen in the [010] direction is 4.76 Å and that in the [01 $\bar{1}$] direction is 6.44 Å. Among the low-index facets of SnO₂, the atomic arrangement of SnO₂(001) (Figure 6a) presents the best matching lattice for SA(100). The lattice mismatch value is very small along the SnO₂ [010] direction, -0.42% $\{(4.74-4.76 \text{ Å})/4.76 \text{ Å}\}$, in parallel with the SA [010] direction. The lattice mismatch is somewhat larger along the SnO₂ [110] direction, 4.04% $\{(6.70-6.44 \text{ Å})/6.44 \text{ Å}\}$, in matching the SA [01 $\bar{1}$] direction. Tilting toward either [010] or [110], not both, the 4-fold symmetry of SA(100) plane provides four orthogonal directions for the SnO₂ wire to align. The rectangular grid pattern in Figure 1a can be understood when the four orthogonal directions are equally probable during growth.

The atomic template of SA(110) presents a more complicated symmetry for the SnO₂ crystal. The lattice of SnO₂-(101) facet matches that of SA(110) facet, as illustrated in Figure 7. A small mismatch can be found along the SnO₂ [$\bar{1}01$] direction (\parallel SA [$\bar{1}10$]), -0.17% $\{(5.71-5.72 \text{ Å})/5.72 \text{ Å}\}$. But the mismatch is larger in its perpendicular direction SA [00 $\bar{1}$], 9.22% $\{(4.74-4.34 \text{ Å})/4.34 \text{ Å}\}$. The other probable direction for wire tilting is along the direction of SA [221] or [22 $\bar{1}$], and the mismatch 6.00% $\{(7.42-7.00 \text{ Å})/7.00 \text{ Å}\}$, as shown in Figure 7c. When the wires are tilted toward the two directions of SA [$\bar{1}10$] and [22 $\bar{1}$] (or [221]) on one surface, this planar alignment creates the herringbone

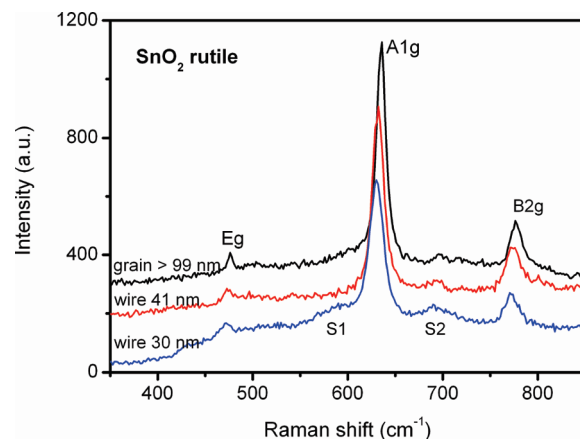


Figure 8. Raman spectra of two SnO₂NW samples with the average size of 30 and 41 nm on SA(100), and the spectrum of the SnO₂ powder reference, which was sintered at 1000 °C for 8 h so that the crystallite size is sufficiently large. Note the peak shifting and broadening for the samples of small wire size. The Au sputtering time is listed in Table 1.

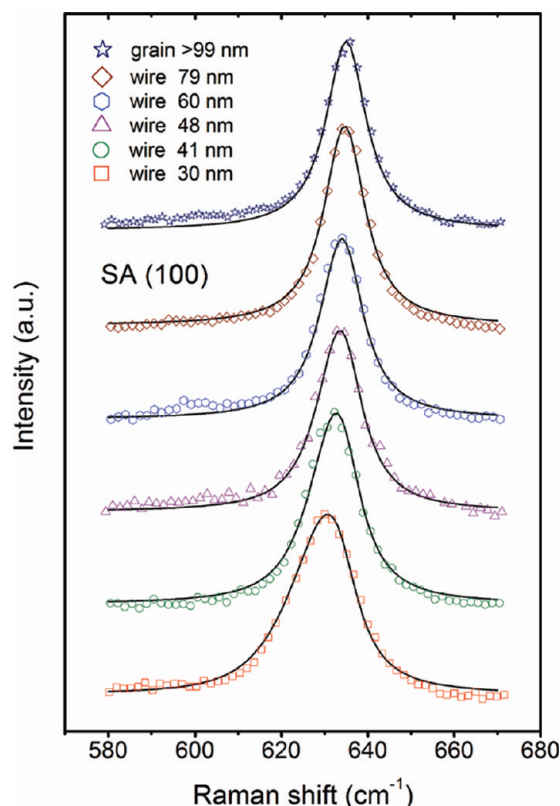


Figure 9. A_{1g} mode of SnO₂NW of various average wire sizes, grown on SA(100). Note the peak shifting and broadening increase with decreasing wire size. The Au sputtering time is listed in Table 1.

pattern of Figure 1b, whose wire projections on SA are not orthogonal.

3.3. Wire Size Manipulation and Raman Analysis. The wire size is a crucial structural variant in the potential applications of SnO₂NW. For gas sensing, the sensor signal increases when the SnO₂ wire diameter is approaching the width of electron depletion region.³⁻⁵ For the field effect transistor based on single SnO₂ nanowire, the capacitance of the back gate is directly related to the lateral dimension of the nanowire.¹⁰ For field emission, the geometric enhancement

Table 1. Values of Redshift and Line Width of the A_{1g} Mode for SnO_2NW , and the Correlated Wire Size Using the SC Model^a

sputtering time (s)	A_{1g} position (cm^{-1})	FWHM (cm^{-1})	peak shift (cm^{-1})	L_1 (SC) (nm)	size (FESEM) (nm)
1000 °C annealed powder	634.9	11.1	0.0		> 99
SA(100)					
40	634.6	11.2	0.3	79	82 ± 4
30	633.9	11.7	1.0	60	63 ± 3
20	633.4	12.2	1.5	48	47 ± 4
10	632.4	13.5	2.5	41	41 ± 4
3	629.9	16.9	5	30	28 ± 3
SA(110)					
40	634.5	11.2	0.4	80	83 ± 4
30	634.3	12.4	1.6	57	55 ± 4
20	632.9	12.8	2.0	46	49 ± 3
10	631.6	14.7	3.3	38	40 ± 3
3	630.2	16.8	4.7	30	32 ± 3

^a The nanowires are grown on two substrates of SA(100) and (110), sputtered with the Au layer for seeding.

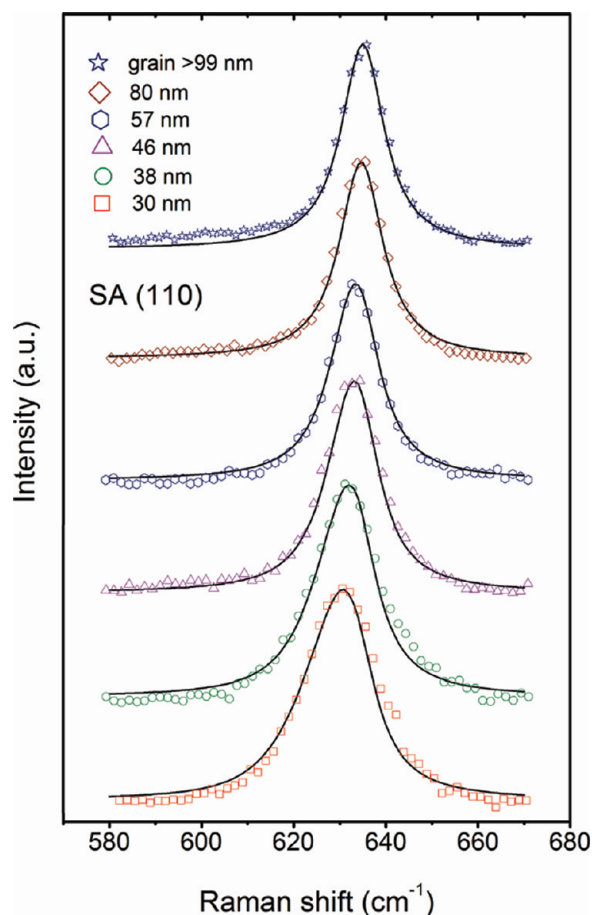


Figure 10. A_{1g} mode of SnO_2 nanowires of various average wire sizes, grown on SA(110). Note the peak shifting and broadening increase with decreasing wire size. The Au sputtering time is listed in Table 1.

factor of Fowler–Nordheim law is connected to the radius of wire tip.²⁷ In this study, we manipulate the wire size via controlling the film thickness of sputtered gold, which was dewetted into gold droplets to guide the wire growth. Quantitatively, the average wire size has been adjusted in the range of 30–80 nm through varying the Au layer thickness from 0.5 to 7.1 nm, while fixing other growth parameters. More precise control on wire size may require a full understanding of the growth mechanism of SnO_2NW . The mechanism of gold mediated growth has been discussed in the growth of Si, Ge, GaAs, MgO nanowires.^{25,26,28–30}

The one-dimensional SnO_2 crystal adopts the tetragonal rutile structure with point group D_{4h} ¹⁴ and space group $P4_2/mmm$. According to the factor group analysis, four first-order Raman active modes of $A_{1g} + B_{1g} + B_{2g} + E_g$ are allowed for the rutile crystal. Among them, the A_{1g} , B_{1g} , and B_{2g} modes are nondegenerated, whereas the E_g mode is doubly degenerated. For SnO_2 nanowires and particles, $A_{1g} + B_{2g} + E_g$ have been observed at 100–800 cm^{-1} .^{15,31–33} Figure 8 illustrates two typical Raman spectra of SnO_2NW at 400–800 cm^{-1} , along with the Raman spectrum of SnO_2 powder of large crystals. The SnO_2 powder was annealed, such that its crystals are free from the confined vibration effects. Raman shifts for the sample of SnO_2 large particles are observed at 476, 635, 776 cm^{-1} . These peak positions are in good agreement with the reported values at 479 cm^{-1} (E_g), 638 cm^{-1} (A_{1g}), and 779 cm^{-1} (B_{2g}) for the sample of SnO_2 particles with crystal size ~ 110 nm, measured by Dieguez et al.³¹ For some nanowires samples, in addition to the three distinct peaks, two weak features at ~ 580 and ~ 690 cm^{-1} could be present. These weak features are evident for the sample of relatively thin wires. The two minor features, also observed in other papers,^{31,34,35} might originate from the surface imperfections.¹⁹

Figure 8 also indicates the Raman lines of the nanowires sample exhibit measurable line shifts and broadening. It has been established that the decrease in semiconductor crystal size leads to down shift and broadening of Raman peaks if the phonon vibration of nanocrystals is confined in space by crystallite boundaries or surface disorders. The confinement causes an uncertainty in the wave vector of the phonons and results in redshift and line broadening. A crystal size parameter can be correlated using the confined vibration mode when fitted to the spatial correlation (SC) model, which was proposed by Richter et al.³⁶ and extended by Campbell and Fauchet for various geometries.³⁷ Therefore, analyzing the Raman peaks of a well-crystalline SnO_2NW sample can correlate its wire size, which is the essential one-dimensional attribute as discussed earlier.

Following the SC model, the intensity of the first-order Raman scattering, $I(\omega)$ at frequency ω , is³⁷

$$I(\omega) \cong \int \frac{d^3q |C(0, \mathbf{q})|^2}{[\omega - \omega(\mathbf{q})]^2 + (\Gamma/2)^2} \quad (1)$$

where $\omega(\mathbf{q})$ is the phonon dispersion curve being a function of the wave vector \mathbf{q} , Γ is the natural line width, and $C(0, \mathbf{q})$ is the Fourier coefficient of the phonon confinement function. Using the Gaussian confinement function and considering

a column shaped crystal, the Fourier coefficient $|C(0, \mathbf{q})|^2$ is rewritten as^{37,38}

$$|C(0, q_1, q_2)|^2 \cong \exp(-q_1^2 L_1^2 / 16\pi^2) \exp(-q_2^2 L_2^2 / 16\pi^2) \left| 1 - \operatorname{erf} \left(\frac{iq_2 L_2}{\sqrt{32}\pi} \right) \right|^2 \quad (2)$$

where L_1 is the wire diameter and L_2 the wire length. For SnO₂NW, the wire diameter L_1 is far less than the wire length L_2 . Hence the intensity of first-order Raman scattering is simplified

$$I(\omega) \propto \int \exp \left(\frac{-q^2 L_1^2}{16\pi^2} \right) \frac{d^3 q}{[\omega - \omega(q)]^2 + (\Gamma/2)^2} \quad (3)$$

For $\omega(q)$, the analytical relation is adopted, based on a one-dimensional linear-chain model, $\omega(q)^2 = A + \{A^2 - B[1 - \cos(\pi q)]\}^{1/2}$. Values of A and B are taken from fitting the A_{1g} line profile of the SnO₂ powder sample of large crystals, $A = 2.020 \times 10^5 \text{ cm}^{-2}$, $B = 8.811 \times 10^9 \text{ cm}^{-4}$.

Among the three Raman modes of E_g, A_{1g}, and B_{2g}, the A_{1g} line is most suitable for further analysis to correlate the wire diameter L_1 , because of its high intensity. As the sputtering time of gold layer varies from 3 to 40 s, the A_{1g} line profile exhibits a systematic variation in mode shift and line broadening. Figure 9 presents the experimental data of the shifting A_{1g} mode for the SnO₂NW grown on SA(100) and their fitting curves, using eq 3. Values of redshift and broadening are listed in Table 1. The redshift is expressed as the wavenumber difference between SnO₂NW and the reference SnO₂ powder. The broadening is expressed as the full width at half-maximum (FWHM), also in wavenumber. Also tabulated are the values of fitted wire size L_1 and the average wire size observed using FESEM. Figure 10 presents the Raman spectrum and the theoretical fit of A_{1g} mode for the SnO₂NW grown on SA(110). Values of redshift, FWHM, the SC fitted wire size, the FESEM wire size are also listed in Table 1. For the same sputtering time, the difference is less than 3 nm between the two fitted wire sizes of SA(100) and SA(110). The 3 nm difference in the size data is within the standard deviation of wire size distribution, suggesting the substrate type is not a factor in the wire size control.

4. Conclusions

We have studied the structural details near the roots of SnO₂NW, and tuned the average wire size via controlling the sputtered gold layer of thickness. The organized pattern of relatively short wires clearly indicates that the heteroepitaxy dictates the wire arrangement on the substrate. The X-ray diffraction analysis and the TEM analysis reveal that SnO₂ nanowires are grown with the (001) facet stacking up along the growth direction [101] on SA(100). The wire body is enclosed by {010} and {101} facets, which envelop the rectangular cross-section for the wire. The growth of SnO₂ nanowires on SA(110) is very similar, except that the SnO₂(101) facet matches the sapphire (110) facet preferentially. Hence the SnO₂ crystal lengthens in the [100] direction and is enclosed by the perpendicular facets of {010} and {001}. The average wire size of SnO₂NW can be manipulated in the range of 30–80 nm through varying the sputtering time of gold. The results of crystal size analysis, based on the confined lattice vibration of Raman signal, conclude that the wire size depends on the gold droplet size, not the type of substrate.

Acknowledgment. The authors thank the National Science Council of Taiwan for financial support of this work through Project NSC96-2221-E-011-164-MY3.

References

- (1) Lu, J. G.; Chang, P.; Fan, Z. *Mater. Sci. Eng., R* **2006**, *52*, 49–91.
- (2) Cheng, Y.; Xiong, P.; Yun, C. S.; Strouse, G. F.; Zheng, J. P.; Yang, R. S.; Wang, Z. L. *Nano Lett.* **2008**, *8*, 4179–4184.
- (3) Sysoev, V. V.; Goschnick, J.; Schneider, T.; Strelcov, E.; Kolmakov, A. *Nano Lett.* **2007**, *7*, 3182–3188.
- (4) Sysoev, V. V.; Button, B. K.; Wepsiec, K.; Dmitriev, S.; Kolmakov, A. *Nano Lett.* **2006**, *6*, 1584–1588.
- (5) Jung, T. H.; Kwon, S. I.; Park, J. H.; Lim, D. G.; Choi, Y. J.; Park, J. G. *Appl. Phys. A: Mater. Sci. Process.* **2008**, *91*, 707–710.
- (6) Qin, L.; Xu, J.; Dong, X.; Pan, Q.; Cheng, Z.; Xiang, Q.; Li, F. *Nanotechnology* **2008**, *19*, 185705.
- (7) Kuang, Q.; Lao, C.; Wang, Z. L.; Xie, Z.; Zheng, L. *J. Am. Chem. Soc.* **2007**, *129*, 6070–6071.
- (8) Hernandez-Ramirez, F.; Prades, J. D.; Tarancon, A.; Barth, S. Casals, O.; Jimenez-Diaz, R.; Pellicer, E.; Rodriguez, J.; Juli, M. A.; Romano-Rodriguez, A.; Morante, J. R.; Mathur, S.; Helwig, A.; Spannake, J.; Mueller, G. *Nanotechnology* **2007**, *18*, 495501.
- (9) Dmitriev, S.; Lilach, Y.; Button, B.; Moskovits, M.; Kolmakov, A. *Nanotechnology* **2007**, *18*, 055707.
- (10) Dattoli, E. N.; Wan, Q.; Guo, W.; Chen, Y.; Pan, X.; Lu, W. *Nano Lett.* **2007**, *7*, 2463–2469.
- (11) Ma, L. A.; Ye, Y.; Hu, L. Q.; Zheng, K. L.; Guo, T. L. *Physica E* **2008**, *40*, 3127–3130.
- (12) Zhang, Y.; Yu, K.; Li, G.; Peng, D.; Zhang, Q.; Hu, H.; Xu, F.; Bai, W.; Ouyang, S.; Zhu, Z. *Appl. Surf. Sci.* **2006**, *253*, 792–796.
- (13) Pan, Z. W.; Dai, Z. R.; Wang, Z. L. *Science* **2001**, *291*, 1947–1949.
- (14) Dai, Z. R.; Gole, J. L.; Stout, J. D.; Wang, Z. L. *J. Phys. Chem. B* **2002**, *106*, 1274–1279.
- (15) Wang, J. X.; Liu, D. F.; Yan, X. Q.; Yuan, H. J.; Ci, L. J.; Zhou, Z. P.; Gao, Y.; Song, L.; Liu, L. F.; Zhou, W. Y.; Wang, G.; Xie, S. S. *Solid State Commun.* **2004**, *130*, 89–94.
- (16) Ma, Y. J.; Zhou, F.; Lu, L.; Zhang, Z. *Solid State Commun.* **2004**, *130*, 313–316.
- (17) Mathur, S.; Barth, S. *Small* **2007**, *3*, 2070–2075.
- (18) Liu, Z.; Zhang, D.; Han, S.; Li, C.; Tang, T.; Jin, W.; Liu, X.; Lei, B.; Zhou, C. *Adv. Mater.* **2003**, *15*, 1754–1757.
- (19) Zhou, J. X.; Zhang, M. S.; Hong, J. M.; Yin, Z. *Solid State Commun.* **2006**, *138*, 242–246.
- (20) Zhang, D. F.; Sun, L. D.; Yin, J. L.; Yan, C. H. *Adv. Mater.* **2003**, *15*, 1022–1025.
- (21) Zheng, M.; Li, G.; Zhang, X.; Huang, S.; Lei, Y.; Zhang, L. *Chem. Mater.* **2001**, *13*, 3859–3861.
- (22) Vayssieres, L.; Graetzel, M. *Angew. Chem., Int. Ed.* **2004**, *43*, 3666–3670.
- (23) Gu, F.; Wang, S.; Cao, H.; Li, C. *Nanotechnology* **2008**, *19*, 095708.
- (24) Nguyen, P.; Ng, H. T.; Kong, J.; Cassell, A. M.; Quinn, R.; Li, J.; Han, J.; McNeil, M.; Meyyappan, M. *Nano Lett.* **2003**, *3*, 925–928.
- (25) Kodambaka, S.; Hannon, J. B.; Tromp, R. M.; Ross, F. M. *Nano Lett.* **2006**, *6*, 1292–1296.
- (26) Kwak, D. W.; Cho, H. Y.; Yang, W. C. *Physica E* **2007**, *37*, 153–157.
- (27) Yang, Y. H.; Wang, B.; Xu, N. S.; Yang, G. W. *Appl. Phys. Lett.* **2006**, *89*, 043108.
- (28) Wang, D.; Dai, H. *Appl. Phys. A: Mater. Sci. Process.* **2006**, *85*, 217–225.
- (29) Harmand, J. C.; Patriarche, G.; Pere-Laperne, N.; Merat-Combes, M. N.; Travers, L.; Glas, F. *Appl. Phys. Lett.* **2005**, *87*, 203101.
- (30) Yanagida, T.; Nagashima, K.; Tanaka, H.; Kawai, T. *J. Appl. Phys.* **2008**, *104*, 016101.
- (31) Dieguez, A.; Romano-Rodriguez, A.; Vila, A.; Morante, J. R. *J. Appl. Phys.* **2001**, *90*, 1550–1557.
- (32) Luo, S. H.; Wan, Q.; Liu, W. L.; Zhang, M.; Song, Z. T.; Lin, C. L.; Chu, P. K. *Prog. Solid State Chem.* **2005**, *33*, 187–292.
- (33) Wang, W.; Xu, C.; Wang, G.; Liu, Y.; Zheng, C. *J. Appl. Phys.* **2002**, *92*, 2740–2742.
- (34) Wang, B.; Yang, Y. H.; Wang, C. X.; Yang, G. W. *J. Appl. Phys.* **2005**, *98*, 073520.
- (35) Liu, Y.; Liu, M. *Adv. Funct. Mater.* **2005**, *15*, 57–62.
- (36) Richter, H.; Wang, Z. P.; Ley, L. *Solid State Commun.* **1981**, *39*, 625–629.
- (37) Campbell, I. H.; Fauchet, P. M. *Solid State Commun.* **1986**, *58*, 739–741.
- (38) Korotcov, A.; Hsu, H. P.; Huang, Y. S.; Tsai, D. S. *J. Raman Spectrosc.* **2006**, *37*, 1411–1415.